J. Fluid Mech. (2005), *vol.* 528, *pp.* 297–321.
doi:10.1017/S0022112004002460 Printed in the United Kingdom

Use of an axial nose-tip cavity for delaying ablation onset in hypersonic flow

By SIDRA I. SILTON† AND DAVID B. GOLDSTEIN

Department of Aerospace Engineering and Engineering Mechanics,
The University of Texas at Austin, Austin, TX 78712, USA

(Received 22 July 2003 and in revised form 13 September 2004)

A forward-facing cavity is examined as a means of reducing the severe heating and delaying ablation onset at the nose-tip of a hypersonic vehicle. Whereas previous studies have concentrated on the nature of flow-induced Hartmann-whistle oscillations or on heating rates alone, the present study addresses the effect of the cavity on ablation onset times through experiments and coupled flow field/heat conduction simulation. Using our previously developed experimental technique, a parametric study is undertaken to optimize the forward-facing cavity geometry for the most delayed ablation onset. The geometric parameters of cavity length, lip radius and diameter are independently optimized for a given nose-tip diameter. Then using benchmarked linked flow field/heat conduction simulations, numerical simulations are conducted for each parametrically optimized configuration in order to investigate the flow physics. The impact of the forward-facing cavity on aerodynamic drag is also considered.

1. Introduction

Hypersonic vehicles are exposed to severe heating which often leads to shape changes due to material ablation. For example, at standard sea level conditions, ablation of tungsten nose-tips for long-rod anti-armour penetrators typically begins to occur at a velocity between $2.0\,\mathrm{km\,s^{-1}}$ (Mach 5.9) and $2.5\,\mathrm{km\,s^{-1}}$ (Mach 7.3) (Reinecke & Guillot 1995; Reinecke & Sherman 1993). Ablation shape changes must be minimized when they produce unacceptable perturbations in the aerodynamics and the resultant vehicle flight path. Thus, it is desirable to find ways to delay ablation onset, decrease the rate of ablation, or devise a way to ensure ablation is uniform. The delay of ablation onset is of particular importance for vehicles having extremely short flight times and promoting such a delay is the primary goal of the present study.

The introduction of a forward-facing cavity in the nose-tip of a hypersonic projectile is known to cause bow shock oscillations (Hartmann & Troll 1922; Johnson 1959; Bastianon 1968; Bohachevsky & Kostoff 1972). Forward-facing cavities have been of interest over the past 15 to 20 years as a possible way of reducing nose-tip heating of hypersonic projectiles. Work previous to 1990 has be reviewed by Silton (2001).

Studies conducted in the early 1990s examined the introduction of a forward-facing cavity specifically to reduce local heating at the cavity lip as compared to a similar spherical nose-tip having no cavity (Yuceil 1995; Engblom 1996). In time-accurate numerical simulations (Engblom *et al.* 1997), resonant bow shock oscillations were

† Present address: US Army Research Laboratory, AMSRD-ARL-WM-BC, Aberdeen Proving Ground, MD 21005, USA.

obtained if either free-stream fluctuations were present or a sufficiently deep cavity was employed even without the presence of free-stream fluctuations. Experimental studies conducted in a quiet Mach 4 tunnel confirmed that there is a critical cavity length-to-diameter ratio, beyond which bow shock oscillations are self-sustaining (Engblom *et al.* 1997; Ladoon, Schneider & Schmisseur 1998). Engblom & Goldstein (1996) showed numerically that the local heat flux everywhere on the surface was reduced when strong longitudinal pressure oscillations within the cavity induced large bow shock oscillations. As the bow shock moved downstream toward the cavity, the relative Mach number decreased and allowed relatively cool gas to enter the cavity. Then as the bow shock moved upstream away from the cavity, the relative Mach number increased. The hot gas present behind the shock was convected away from the the cavity lip by the cooler gas leaving the cavity. See Engblom (1996) for an explanation of a possible mechanism for the shock unsteadiness.

The present paper presents results from a joint numerical/experimental study that attempted to develop an understanding of the unsteady flow physics that occur when a forward-facing cavity is introduced into the nose-tip of a hypersonic projectile. In particular, the effect of the cavity geometry on the surface heating and, therefore, ablation onset time are investigated. Section 2 discusses the experimental methodology wherein a low temperature ablator is used in our Mach 5 facility. The numerical methodology that was developed to couple the flow field and heat transfer solutions is introduced in § 3. The experimental and numerical results are presented and discussed in § 4.

2. Experimental methodology

All experiments were conducted in the Mach 5 blow-down wind tunnel at The University of Texas at Austin J. J. Pickle Research Center Wind Tunnel Laboratory. As this is not a high enthalpy tunnel, the following methodology was developed for studying ablation onset using a low temperature ablator (Silton & Goldstein 2000; Silton 2001).

2.1. *Wind tunnel*

The wind tunnel's test section was a rectangle 152.4 mm wide, 177.8 mm high, and 685.8 mm long. A floor slot was used to mount the models, and circular sidewall windows allowed for video imaging. A compressed air storage system (at 17.24 MPa) allowed for run times of up to one minute without a significant drop in the tunnel stagnation pressure. The incoming air was heated by two banks of Nichrome wire resistive heaters located upstream of the stagnation chamber.

The tunnel was operated at a nominal stagnation pressure, P_{stag}, and temperature, T_{stag}, of 2.30 MPa and 370 K, respectively. For a free-stream Mach number of 4.91, these stagnation conditions correspond to a free-stream unit Reynolds number of 5.0×10^6 mm^{-1}, and a free-stream velocity, static air pressure (P) and static temperature (T) of 787 m s^{-1}, 4694 Pa and 64 K, respectively.

2.2. *Models*

The nose-tip of the hypersonic projectile of interest is typically a blunted cone-cylinder configuration with approximately a 7° cone half-angle. However, since the focus of this work was on the stagnation region and the sonic line occurs upstream of the conical region of the projectile (i.e. the conical region does not effect the stagnation region), the projectile nose was modelled as a sphere-cylinder (Yuceil

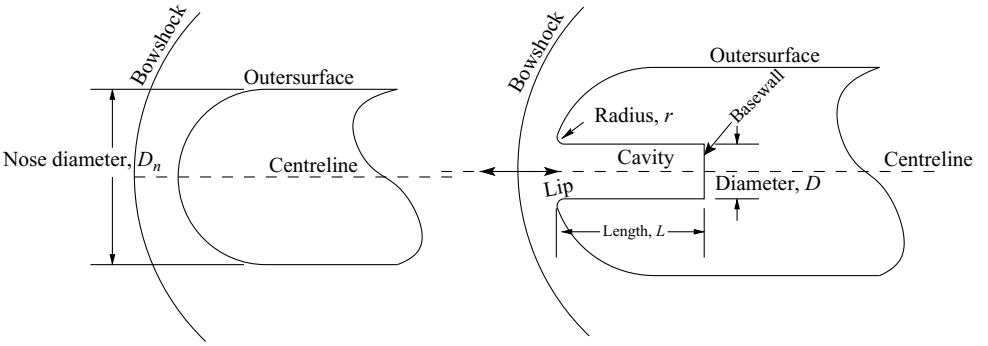

FIGURE 1. Basic model geometries with and without a cavity. (*a*) Hemisphere–cylinder (baseline); (*b*) Axial cavity – rounded lip.

1995; Engblom 1996; Silton & Goldstein 2000). Thus, the basic model geometry was a hemispherically-blunted cylinder with a streamwise cylindrical nose cavity (figure 1).

The material chosen for the model needed to ablate at low temperatures, as the stagnation temperature was considerably lower than in actual flight. Water ice was chosen as a suitable material. It is inexpensive, well-characterized, easily moulded, melts nearly 100 K below T_{stag}, and is neither toxic nor flammable.

Several models, with varying geometry, were used over the course of the study. Each ice model was frozen in a polished aluminium mould. Each mould was designed to create a model with a nose diameter, D_n, of 25.4 mm. The centre of the mould was bored out to accommodate an insert that allowed the formation of the appropriate cavity geometry (cavity diameter (D), cavity length (L), and cavity lip radius (r)).

The mould was filled with distilled water and chopped fibreglass threads (see Silton & Goldstein 2000). A brass spindle was placed in the mould to extract the ice model from the mould as well as provide a base with which to attach the model to the sting adapter. The filled mould was placed in liquid nitrogen (LN2) vapours for 20 minutes until the water was completely frozen. The spindle with the ice model attached was then forcibly pulled free of the mould. The spindle, with the completed ice model attached, was placed back in the LN2 vapours for an additional one to two hours to gradually reduce the temperature of the ice to 78 K, the boiling point of LN2. Finally, just prior to the run, the model was fully immersed in LN2 until boiling ceased. This delayed the onset of ablation for several seconds into the tunnel run and established a known uniform initial temperature.

2.3. *Experimental procedure*

Shielding of the model was required to protect the ice from irregular heating during start-up of the wind tunnel. The shield consisted of two parts, a reusable brass outer shroud and an expendable wood shroud cap. This provided sufficient insulation of the ice from the flow field as there was no direct contact with the flow-warmed shield.

The precooled outer shroud was positioned over the ice model and spindle and placed in the LN2 to ensure a uniform temperature. The cooled assembly was screwed into the precooled sting adapter, the shroud cap positioned, and a long tapered pin fitted in place. This pin was inserted up through the tunnel floor and outer shroud, fitted into a hole in the bottom of the spindle, and held in place with a solenoid release mechanism. The wind tunnel was quickly closed and started to minimize model heating prior to the tunnel reaching steady-state conditions.

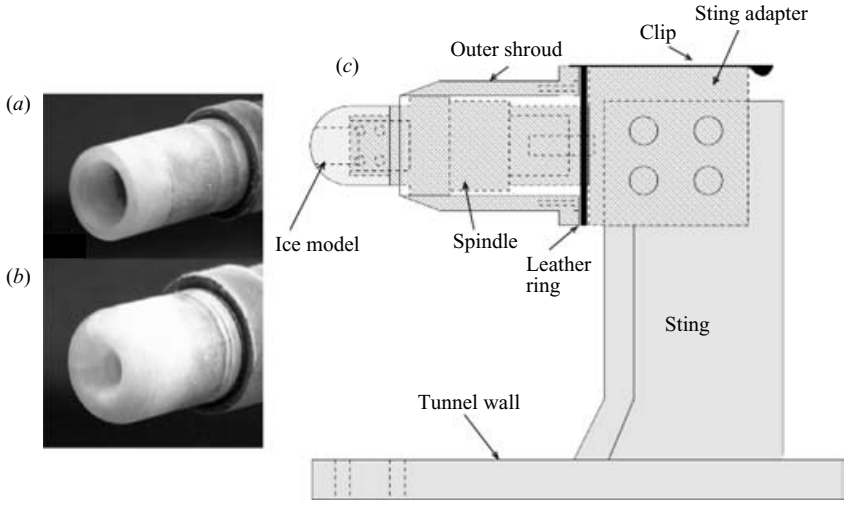

FIGURE 2. Photos of (*a*) $r = 1.90$ mm, $D = 17.8$ mm cavity (case 7) and (*b*) $r = 4.44$ mm, $D = 7.6$ mm cavity (case 6). (*c*) Schematic of assembled wind-tunnel structure with baseline ice model exposed.

Once the tunnel started and stabilized (15–20 s into the run), the solenoid was retracted allowing the pin to be pulled free (by weights attached to the bottom of the pin) and the outer shroud to slide back over the spindle (owing to unbalanced pressure forces). The shroud cap came loose and flew off downstream, exposing the ice model (figure 2) at time zero ($t = 0$ s).

2.4. *Video imaging process*

During the length-to-diameter ratio, L/D, parameter study, a Canon L1 Hi-8 video camera having a horizontal resolution of 400+ lines and a framing rate of 30 Hz imaged the model. These movies were digitized using Macintosh Movie Player. For the remainder of the parameter study, a Canon GL1 digital video camera (250 000 effective pixels, 30 Hz framing rate) was used.

A reference image, when the model first became completely exposed to free-stream conditions ($t = 0$ s), was determined to within ± 0.05 s during post-processing. Each subsequent image was subtracted from the reference image and examined to determine whether ablation onset had occurred.

3. Numerical methodology

The numerical assumptions and procedure summarized below were developed and validated during the benchmark study (see Silton & Goldstein 2000; Silton 2001). Numerical body geometry, material properties and free-stream conditions were consistent with those of the experiments.

3.1. *Computer code description*

The commercial finite-volume computer code, INCA v2.5 (Imlay *et al.* 1998), was used for the fluid dynamics (flow field) portion of this study. This code was also used in similar previous studies by Engblom (1996), Engblom *et al.* (1996, 1997) and Silton & Goldstein (2000). INCA is second order in time and space and uses flux splitting with upwinding to capture strong shocks. The finite-element computer program, COYOTE

v2.5 (Gartling & Hogan 1994), was used to solve the solid-body heat-conduction portion of the problem. COYOTE has previously been used in conjunction with a flow-field solver similar to INCA (Hassan, Kuntz & Potter 1998; Kuntz, Hassan & Potter 1999) as user supplied subroutines allow for a relatively easy transfer of boundary conditions.

Algebraic grids were created for the external fluid domain using GRIDALL (1994). Unstructured grids were created for the solid body using FASTQ (Blacker 1988). See the supporting documentation for more complete code descriptions.

3.2. *Numerical assumptions*

The flow-field calculations assumed flow of a thermally and calorically perfect gas. Axisymmetry was assumed because the bow shock had previously been found to oscillate axisymmetrically in front of the deep cavities of interest here (Yuceil 1995; Yuceil & Dolling 1996) and pressure oscillations at the cavity base wall have been found to be planar (Yuceil 1995; Engblom *et al.* 1996; Yuceil & Dolling 1996). This assumption is implemented as a two-dimensional grid with a symmetry plane boundary condition at the centreline.

The flow was assumed to be laminar as preliminary results (Silton 2001) showed that the laminar numerical results agreed with the comparable experimental results. Specifically, experimentally observed ablation onset times were consistent with the numerical results when the laminar flow assumption was used. When the numerical calculations were completed with a turbulent boundary-layer assumption, unrealistically rapid ablation onset times are obtained. Additionally, the free-stream noise present in the blow-down wind tunnel is neglected as the cavity depths of interest here are expected to self-sustain strong bow shock oscillations (Engblom 1996; Engblom & Goldstein 1996).

Finally, the surface temperature for the wall-temperature boundary condition was assumed to be constant. An early estimate for the surface temperature was 100 K. A more realistic surface temperature of 163 K was determined from embedded thermocouples in the baseline hemisphere–cylinder model (Silton 2001). Since a number of the flow-field calculations had already been completed using a constant surface temperature of 100 K, a study was completed to determine the variation in the surface heat flux coefficient when a surface temperature of 163 K was used. The variation in surface heat flux coefficient was minimal. Thus, a constant surface temperature of 100 K was used for the remainder of the study for consistency.

For the solid-body heat-conduction calculations, an axisymmetric body is also assumed. The model was initialized using a uniform temperature (either 100 K or 163 K, as in the above discussion). The thermal properties of the body were assumed to be only those of water ice and do not take into account the (minor constituent) glass fibres or the central brass spindle present in the experiment. Variable material properties used for water density (Hobbs 1974), specific heat (Johnson 1961) and thermal conductivity (Childs, Ericks & Powell 1973) ranged from $934\,\mathrm{kg\,m^{-3}}$, $882\,\mathrm{J\,K\,kg^{-1}}$ and $6.5\,\mathrm{W\,K\,m^{-1}}$, respectively at 100 K to $910\,\mathrm{kg\,m^{-3}}$, $2100\,\mathrm{J\,K\,kg^{-1}}$ and $2.2\,\mathrm{W\,K\,m^{-1}}$, respectively at 273 K.

3.3. *Numerical procedure*

A three order of magnitude difference in characteristic times between the flow field and the solid body exists. Therefore, it is not practical to solve the two parts of the problem simultaneously. Hence, a linking procedure (Silton & Goldstein 2000; Silton 2001) was used.

3.3.1. *Flow-field code procedure*

Over a hemisphere–cylinder body, the flow is steady and the procedure simple. The output files from the steady baseline hemisphere–cylinder flow-field solution were used to obtain the heat flux distribution, $q(x, y)$, over the solid-body surface. This distribution was used to calculate the heat conduction coefficient distribution, $h(x, y)$, from

$$h(x, y) = \frac{q(x, y)}{T_w(x, y) - T_{aw}(x, y)}. \tag{3.1}$$

$T_w(x, y)$ is the wall temperature distribution ($T_w(x, y) = 100\,\mathrm{K}$ when calculating $h(x, y)$). $T_{aw}(x, y)$, the adiabatic wall temperature, was obtained via a separate flow-field calculation assuming an adiabatic wall-boundary condition.

When an axial cavity, 25.4 mm in diameter and 50.8 mm in length ($L/D = 2.0$) or deeper, is introduced into a $D_n = 50.8$ mm nose of a model projectile at Mach 5, the bow shock oscillations are self-sustaining (Engblom 1996). Therefore, the flow field around the body with a nose-tip cavity must be solved in a time-accurate manner.

Generally, one pressure oscillation cycle was solved using 3000–4000 global time steps and 6 subiterations per time step. The computational time requirement (at the converged spatial resolution) was typically 4 hours per cycle on a CRAY T90 and 15–20 hours per cycle on a single processor of an SGI Origin 2000. The solution was assumed periodic once the time-averaged (mean) heat flux, obtained by averaging 50 instantaneous surface heat flux distributions over one complete pressure oscillation cycle, did not change appreciably from one cycle to the next (Engblom 1996). Nearly 90 pressure oscillation cycles were required to obtain a converged solution.

The converged mean heat flux distribution was used to obtain $h(x, y)$ from (3.1). The key assumption here is that, although the heat flux varies drastically during a single oscillation cycle, the surface temperature does not respond nearly that fast. Thus, heat flux averaged over one cycle (with a period of about 1/3000 s) is suitable for computing the solid-body temperature field. The mean adiabatic wall temperature distribution was similarly obtained by averaging the instantaneous adiabatic wall temperature distribution obtained from a second, adiabatic, simulation.

3.3.2. *Heat conduction code procedure*

$T_{aw}(x, y)$ and $h(x, y)$ (§ 3.3.1) were used as boundary conditions for the heat conduction code. The heat conduction code was run from an initial time, t_i, of 0 s. The solution was considered accurate until ablation onset occurred, as changes in material properties and the reduction of mass owing to ablation were not modelled. As such, the simulations were considered complete when a point on the solid body reached its melting point.

The initial time step, $\mathrm{d}t_i$, was 0.01 s and the integration tolerance criteria was set to 1.0×10^{-5} for all geometries (Silton & Goldstein 2000; Silton 2001). These simulations typically required 5–7 hours of computation time on a CRAY SV1. Iterations between the heat conduction code and the flow-field code could be done to update the heat flux and surface temperature boundary conditions, respectively, but was found to be unnecessary.

3.4. *Grid and geometry*

A grid resolution study was conducted for both the flow-field computations and the solid-body heat conduction computations (Silton & Goldstein 2000; Silton 2001). A maximum surface cell thickness of 2.5×10^{-4} mm was used in the flow field for each of the geometries studied herein. For the baseline geometry, a difference in surface heat

Case	Geometry	Picture
1	Baseline hemisphere–cylinder	
2	$D = 10.31$ mm, $L/D = 2.0$, $r = 1.19$ mm	
3	$D = 10.31$ mm, $L/D = 4.0$, $r = 1.19$ mm	
4	$D = 12.7$ mm, $L/D = 4.0$, $r = 1.19$ mm	
5	$D = 12.7$ mm, $L/D = 4.0$, $r = 3.175$ mm	
6	$D = 7.62$ mm, $L/D = 4.0$, $r = 4.445$ mm	
7	$D = 17.78$ mm, $L/D = 4.0$, $r = 1.905$ mm	

TABLE 1. Geometry definitions for numerical investigations with case numbers and representative cross-sections. Case numbers do not correspond to the geometry numbers in Silton (2001).

Case	Zone 1	Zone 2	Zone 3	Zone 4	Zone 5	Solid body
1	200×160					27 300
2	464×79	74×199	74×589	45×74	74×45	94 326
3	458×79	54×174	74×564	59×74	54×45	91 820
4	489×80	74×199	74×589	70×74	74×45	101 703
5	367×174	49×199	74×531	70×74	49×84	73 213
6	458×174	34×199	74×664	60×74	34×101	93 418
7	303×174	74×199	74×398	80×74	74×50	39 227

TABLE 2. Cell distribution for baseline and five zone flow-field grids and total element count for the solid-body grid used in parameter study.

flux of less than 1% was found when these results were compared to results computed on a grid with a maximum surface cell thickness of 1.0×10^{-4} mm. A separate grid resolution study was conducted for the cavity geometry. Again, a maximum surface cell spacing of 2.5×10^{-4} mm was found to be adequate. Maximum differences in surface heat flux occurred at the cavity base where magnitudes were low. Average mean heat flux difference at the lip, where heating is most severe, were only 0.1%.

Use of the flow-field surface cell distribution for the solid-body grid generated an internal grid that more than adequately resolved the solid body; the use of a coarser cell distribution changed the ablation onset time by less than 0.5%. See Silton (2001) for further details of the grid resolution study.

Seven geometries were numerically investigated over the course of this study (table 1). Each cavity geometry used a five zone multi-block flow-field grid (figure 3) comprised of the cell distributions shown in table 2. The total element count for each solid-body grid is also shown in table 2.

4. Results and discussion

A parametric study was conducted to determine the cavity geometry that would most delay the onset of ablation and to clarify the physics of the nose-tip heating. The parameters investigated included L, D and r. The effects of the ratio of cavity length to cavity diameter (L/D) and cavity lip radius to nose wall thickness ($r/(D_n - D)$)

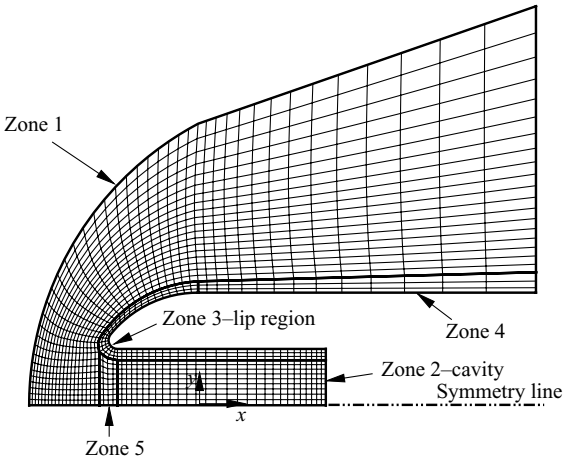

FIGURE 3. Schematic of a five zone flow-field grid used for numerical calculations.

were also investigated. The study was conducted in three phases in a progressive manner. In order to reduce the number of possible combinations, only the value of the parameter which most delayed the onset of ablation in one phase was carried forward to the next phase.

The parametric studies were completed experimentally owing to the relative ease and quickness of creating new experimental geometries as compared to the time and expense of the numerical simulations (Silton & Goldstein 2000; Silton 2001). The best experimental configuration(s) from each parameter study were investigated computationally to determine how the flow physics had been altered.

4.1. *Cavity length*

4.1.1. *Experiments*

An investigation of cavity length was completed first. Two different lip radii, 0.80 mm and 1.19 mm, were investigated in detail. The cavity diameters were 11.1 mm and 10.3 mm, respectively. A range of L values, corresponding to L/D values from 2.0 to 5.0, were investigated. Two or three sets of data (runs) were collected for each geometrical configuration to ensure repeatability and provide a measure of experimental error (taken as the standard deviation).

The very sharp lip cavities ($r = 0.80$ mm) were difficult to produce without defect (i.e. chipped or cracked cavity lips). During post-processing, it was found that any defects in the cavity lip produced substantially shorter ablation onset times even if the images were examined away from the area of the defect. Thus, datum with defects was discarded if sufficient additional data (without defect) were obtained, else the datum was used. Figure 4(*a*) presents the ablation onset times as a function of L/D. These data do not indicate an optimal L/D when $r = 0.80$ mm as there is no definitive maximum. This is probably due to the sharp radius of the cavity lip used. Moreover, all of the models began to ablate well before the simple hemisphere–cylinder body.

The trends in ablation onset time for various L/D for the $r = 1.19$ mm cavity lip were much more definitive (figure 4*b*). Ablation onset was most delayed at $L/D = 4.0$ although $L/D = 3.5$ or $L/D = 4.5$ could also show relatively delayed ablation onset. The variation of ablation onset time with L/D illustrates the trend suggested by

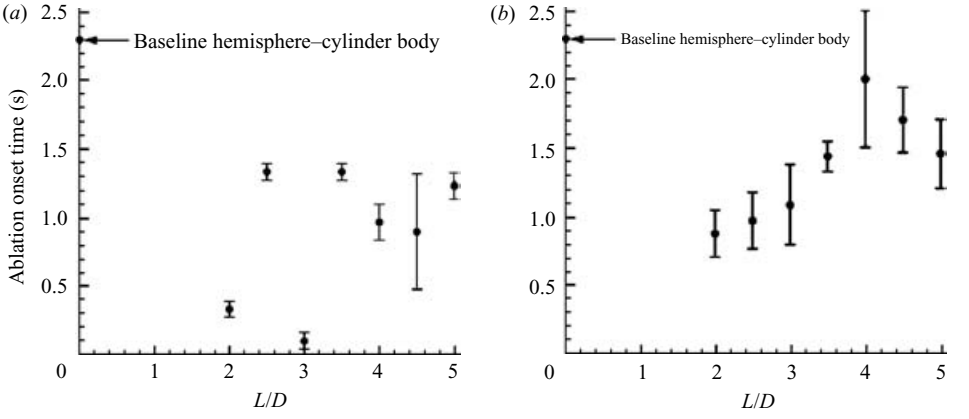

FIGURE 4. Ablation onset times (with error bars) for L/D parameter study with (*a*) $D = 11.1$ m, $r = 0.80$ mm and (*b*) $D = 10.3$ mm, $r = 1.19$ mm.

Engblom (1996); there is a maximum delay in ablation onset for a given D and r as L is varied.

For a constant $L/D = 3.0$ and $r = 1.19$ mm, an increase of cavity diameter from $D = 10.3$ mm to $D = 12.7$ mm has virtually no effect on the experimental ablation onset time (1.10 ± 0.33 s and 1.3 ± 0.1 s, respectively). This suggests that L/D probably has a greater impact on an ablation onset time than does either D or L, individually.

4.1.2. *Computations*

But why should $L/D = 4.0$ significantly delay experimental ablation onset compared to, say, the $L/D = 2.0$ case? To examine the flow physics involved, numerical simulations were run for both geometries. The $L/D = 2.0$ (case 2) simulation required 3000 time steps per pressure oscillation cycle while the $L/D = 4.0$ (case 3) simulation required 4000 time steps for proper temporal resolution (i.e. the solution did not change significantly as the number of time steps was further increased).

The frequency of bow shock oscillation, f, can be analytically determined from Engblom (1996)

$$f = \frac{\sqrt{\gamma R T_{stag}}}{4L^*}, \tag{4.1}$$

where γ is the ratio of specific heats, R is the gas constant, and L^* is the characteristic length of the cavity. As expected, the frequency of bow shock oscillation obtained numerically decreased by slightly less than a factor of two when L/D was doubled. The frequency does not change by exactly a factor of 2 because f depends on $L^* = L + \delta$ (δ is the average bow shock stand-off distance) and δ remains approximately the same. The simulated oscillation frequency for both cases differed from the calculated frequency by no more than 1.75%. This difference was probably due the actual cavity temperature being below that of the stagnation temperature as flow in the cavity is not adiabatic. The bow shock oscillation strength, δ_{rms}, calculated as the root-mean-square variation in shock stand-off distance, decreased slightly when L/D increased, as did the average bow shock speed

$$u_{rel} = 4 f \delta_{rms}. \tag{4.2}$$

Since u_{rel} decreased with increasing L/D, the mean gas stagnation temperature (averaged over one pressure oscillation cycle) of the flow near the mouth of the cavity

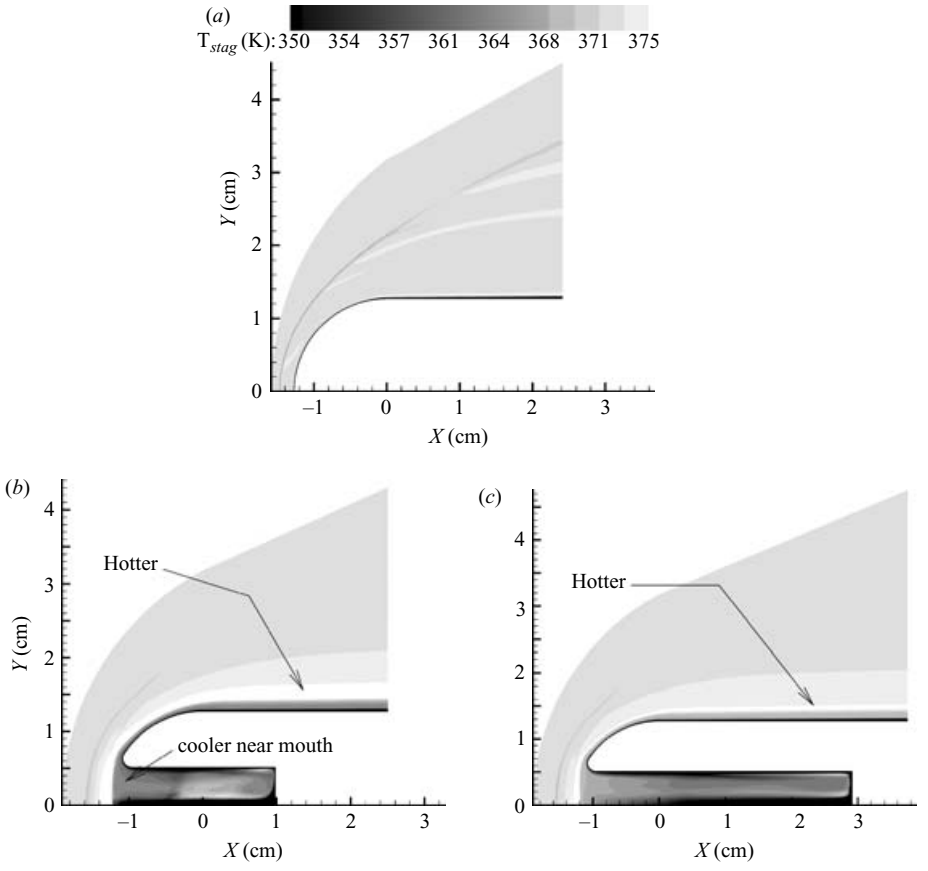

FIGURE 5. Mean stagnation temperature comparison of (*a*) baseline hemisphere–cylinder, (*b*) case 2 and (*c*) case 3.

is expected be lower for case 2 than for case 3 (Engblom 1996). As seen in figure 5, this is indeed the case.

Additionally, both the cases 2 and 3 show a reduction in mean stagnation temperature near the solid surface compared to that of the baseline hemisphere–cylinder geometry (see figure 5). These temperature fields about the cavities indicate that bow shock motion will indeed reduce the mean stagnation temperature behind the shock. In both cavity geometries, a region of increased mean stagnation temperature is also present (the white region), but it is held away from the body by the cooler region. The dark grey region of cooler mean stagnation temperature gas is thicker for case 2, probably because of its higher relative shock velocity.

A decrease in mean surface heat flux near the cavity lip was expected for case 3 compared to case 2 based on the experimental ablation onset times. Yet, the decrease in computational average bow shock speed for this deeper cavity suggested that the mean surface heat flux would actually increase (Engblom 1996) over that for shallow cavity case 2. The mean computational surface heat flux at the lip did, in fact, increase for the deeper cavity.

The bow shock oscillations seen in animations for case 2 had an almost continuous motion, with a short pause in motion at the shock's most downstream position. The nearly continuous bow shock motion is seen in (figure 6). While there is no hesitation

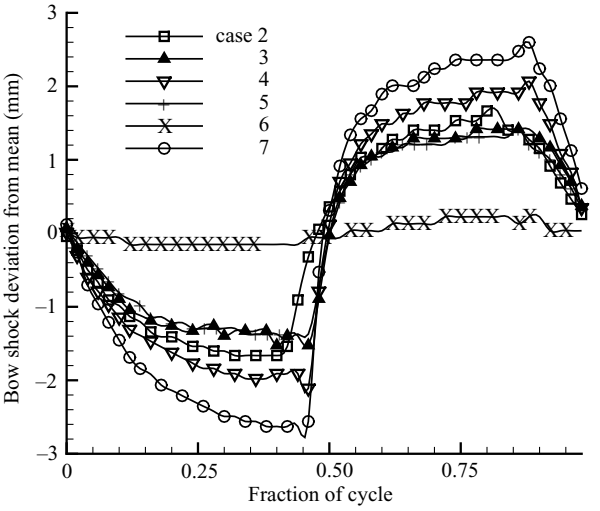

FIGURE 6. Bow shock motion for all computational geometries used during the parameter study plotted as the deviation from the mean bow shock position for that particular geometry. Negative numbers indicate positions aft of mean and positive indicates forward of mean.

in the bow shock motion at its most upstream location for case 2, there does appear to be a short hesitation downstream of the mean location at 30–40% of the oscillation cycle.

For case 3, the bow shock motion is appreciably more abrupt: the bow shock hovered at its most upstream and downstream positions for a majority of the cycle with quick movement in between. The rapid movement between the two positions causes (or is caused by) more rapid expansion and compression of the pressure waves within the cavity. Additionally, the case 3 cavity appears to be deep enough for the pressure waves to have sufficient time to coalesce into a weak shock just inside the cavity mouth at the end of the cavity inflow phase (figure 7*b*). Though large gradients near the inner cavity wall are caused by the coalescence of the pressure waves into a shock, these gradients appear to have a negligible effect on the flow field during the remainder of the oscillation cycle as the gradients dissipate soon after developing. This is probably due to cavity outflow cyclically disgorging the cavity shock, thus minimizing the duration during which strong gradients are present. The upstream bow shock position for case 3 appears to be set by the body 'seen' by the free stream during to the outflow of the cavity (e.g. the stagnation streamline in figure 7*a*). During inflow, the bow shock does not move very far downstream as the streamlines (the instantaneous streamline is everywhere tangent to the instantaneous velocity field) entering the cavity spread a little to form an inlet (figure 7*b*) through which the bow shock apparently cannot be ingested.

The increase in mean surface heat flux for the case 3 flow-field computation corresponds to higher heat flux coefficients input as the boundary condition of the solid-body portion of the simulation. The solid-body heat-conduction solution predicts numerical ablation onset times of 3.2 s and 2.7 s for cases 2 and 3, respectively, when the initial temperature, T_i, is assumed to be 100 K. If, instead, $T_i = 163$ K, and $h(x, y)$ remains fixed, numerical ablation onset times drop to 1.8 s and 1.5 s for cases 2 and 3, respectively. These numerical ablation onset times, regardless of the initial

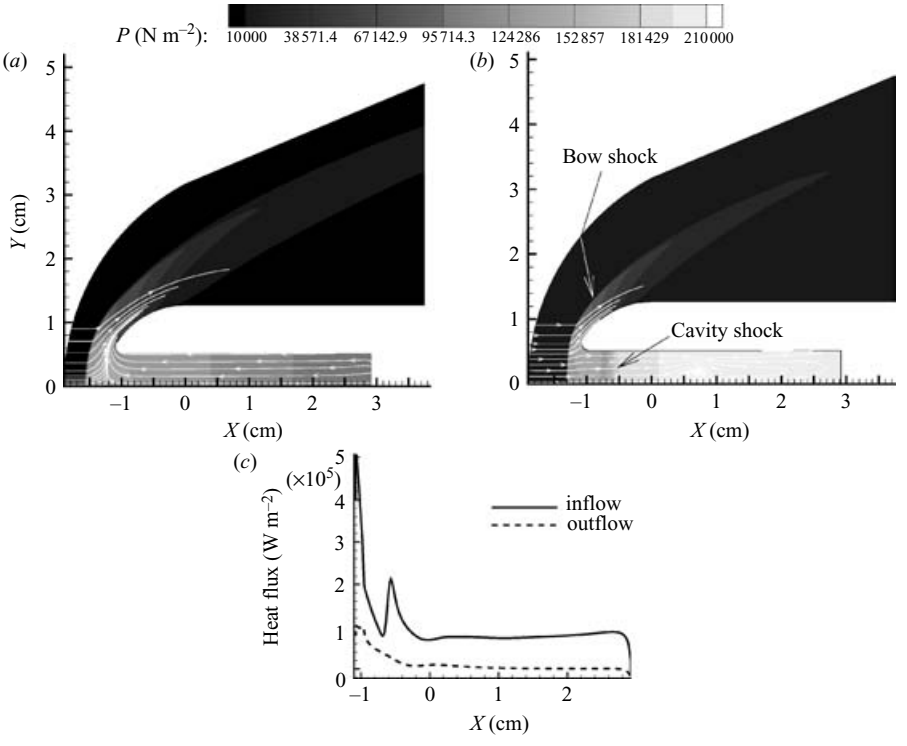

FIGURE 7. Flow-field pressure contours with streamlines for case 3 during (*a*) cavity outflow and (*b*) cavity inflow. (*c*) Corresponding heat flux distributions.

	Ablation onset time (s)					
	Experimental				Numerical	
Case	Run 1	Run 2	Run 3	Average	$T_i = 100\,\mathrm{K}$	$T_i = 163\,\mathrm{K}$
1	1.3	3.5	2.4	2.4	3.73	2.08
2	0.8	1.0	0.87	0.89	3.22	1.79
3	1.57	2.47	–	2.01	2.67	1.46
4	1.47	1.43	1.87	1.59	2.66	1.47
5	3.63	3.03	2.07	2.91	6.60	3.63
6	2.40	3.27	3.13	2.93	5.66	2.93
7	2.77	3.50	3.23	3.17	4.28	2.48

TABLE 3. Comparison of experimental and numerical ablation onset times for geometries on which numerical simulations were completed in the parameter study.

temperature assumed, substantially contradict the experimental trend that shows that case 3 should definitely have a delayed ablation onset compared to that of case 2.

The numerical ablation onset time for case 3 agrees fairly well with the experimental findings: $T_i = 100\,\mathrm{K}$ overpredicts average experimental ablation onset time by 33%, $T_i = 163\,\mathrm{K}$ underpredicts the time by 27%, indicating that the actual initial temperature is probably around 130 K (table 3). Suggesting that the initial temperature is between the two temperatures used for case 3 is not unreasonable as the thermocouple test was conducted only for the baseline case (§ 3.2). However, the

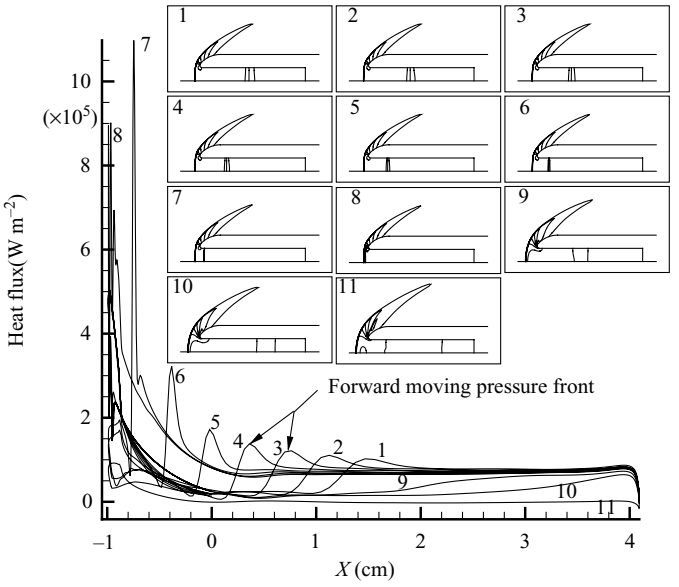

FIGURE 8. Eleven instantaneous heat flux distributions along cavity length and lip for case 4 with corresponding pressure contour plots to show shock position and pressure waves.

numerical ablation onset time for case 2 is too long (at least 100%), regardless of the initial temperature. While it is possible that $T_i \gg 163$ K for case 2, it is more likely that the flow is transitioning to turbulence for the more strongly oscillating case 2 while it remains laminar for case 3. Transition, if it occurs, would cause a large increase in the mean surface heat flux for case 2 and a much faster ablation onset. In fact, a similar cavity geometry ($L/D = 2.0$, $r = 1.0$ mm, $D = 12.7$ mm) had a rapid numerical ablation onset time of 0.94 s when turbulent flow was assumed (Silton & Goldstein 2000; Silton 2001). This agrees remarkably well with the experimental ablation onset time of 0.89 ± 0.7 s for case 2.

The negligible effect, observed experimentally, of increasing the cavity diameter slightly while cavity lip radius and L/D were held constant, was confirmed in numerical simulations. For the numerical comparison, cases 3 and 4 were used. Case 4 used a 20% larger cavity diameter than case 3 and the same lip radius. There was an expected decrease in frequency owing to the increase in cavity length needed to keep $L/D = 4.0$. There was again a slight discrepancy between the simulated frequency and the analytical value of f (4.1) for the larger $D = 12.7$ mm cavity (3.24% low) perhaps because the pressure waves within the larger diameter cavity coalesce into a cavity shock.

The formation of the shock within the cavity and the consequent dramatic increase in the flow-field gradients means that the wall heat flux must be sampled more rapidly at 500 times per cycle, rather than the usual 50, in order to capture all the relevant details along the wall. The instantaneous surface heat flux distribution (figure 8) shows travelling waves that occur as the pressure waves move forward and coalesce into the internal cavity shock. The temperature field at the instant the peak surface heat flux occurs (figure 9) has hot regions associated with the cavity shock. Vorticity is generated in the boundary layer owing to the baroclinic torque created by the large pressure gradient as the shock passes (inset, figure 9). This peak surface heat flux

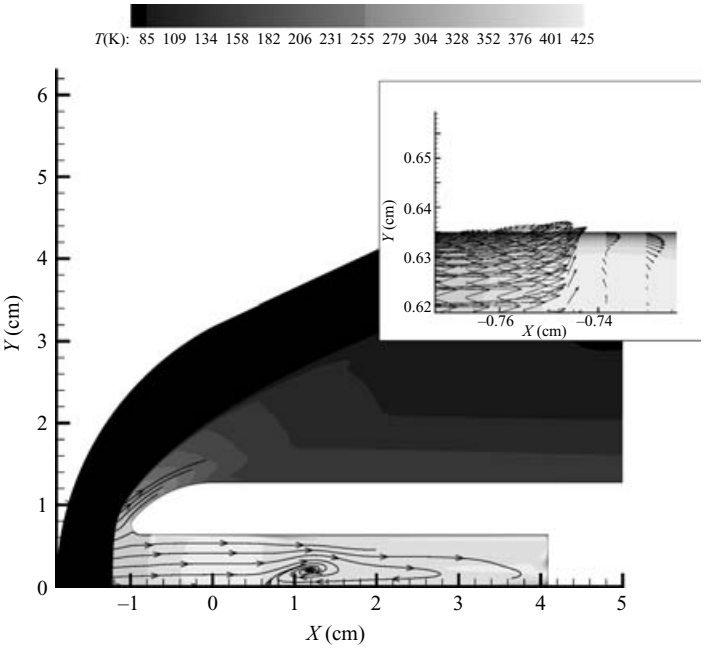

FIGURE 9. Temperature contours of case 4 corresponding to the instantaneous peak heat flux. Inset shows close-up of cavity wall where peak heat flux occurs with velocity vectors.

occurs inside the cavity, not at the time-averaged stagnation point of the lip, and just after (in time) the coalesced shock forms.

A small increase in δ as the cavity diameter increased indicates that the average body shape that the flow sees becomes more blunt. A small increase in the δ_{rms} occurs because of stronger bow shock oscillations and results in a small increase in u_{rel}. This small change in relative velocity caused little change in the value of the mean peak surface heat flux at the lip and virtually no difference in the numerical ablation onset time.

4.2. *Cavity lip radius*

4.2.1. *Experiments*

A study of cavity lip radius was completed next. This study examined six different cavity lip radii, from $r = 1.19$ mm to $r = 3.17$ mm, using the three possible L/D optima (3.5, 4.0, 4.5) from the experimental L/D parameter study. Cavity diameter was set equal to 12.7 mm for all runs and cavity length was measured from the most forward point of the cavity lip. Thus, $r = 3.17$ mm was the bluntest cavity lip possible for the given nose and cavity diameters.

At least three experimental runs were conducted for each geometry. The average ablation onset times were found to be dependent on both cavity lip radius and L/D, as expected (figure 10). The longest times to ablation onset occurred for the most blunt cavities ($r = 3.17$ mm) for each L/D indicating that cavity lip radius had a greater effect on ablation onset times than does cavity L/D (over this small range of L/D). The absolute longest time to ablation onset occurred for $L/D = 4.0$ as indicated by the white in figure 10. Maximum ablation onset times for the other lip radii investigated also occur at $L/D = 4.0$. This confirms the experimental findings of the L/D study, which indicated that $L/D = 4.0$ is somehow best.

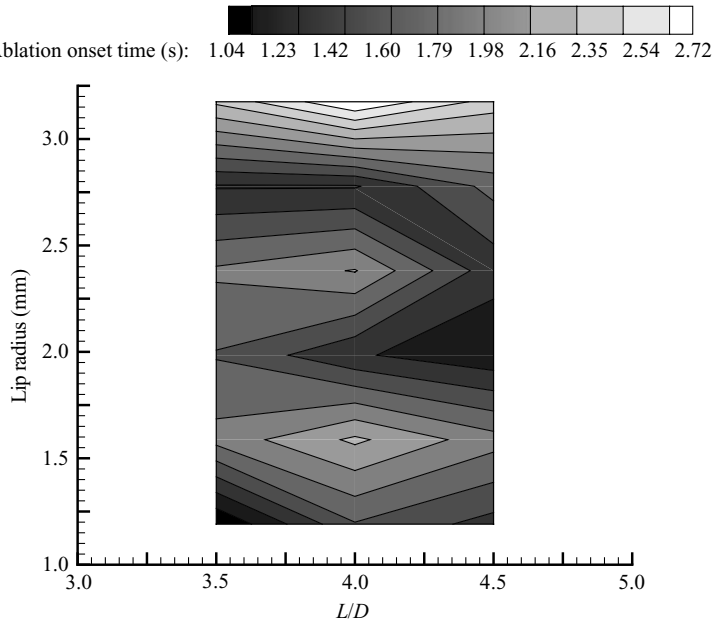

FIGURE 10. Ablation onset times for r parameter study with $D = 12.7$ mm.

4.2.2. *Computations*

In order to determine why $r = 3.17$ mm significantly delayed experimental ablation onset as compared to the other lip radii investigated, a numerical simulation was run for a cavity with $r = 3.175$ mm, $D = 12.7$ mm and $L = 50.8$ mm (case 5). The results of this simulation will be compared to the simulation for the sharper lip of case 4. The new simulation, like that previous, required 3000 time steps per pressure oscillation cycle for proper temporal resolution.

As expected based on (4.1), the frequencies of bow shock oscillation obtained numerically for cases 4 and 5 were very similar (1.5% difference). The difference is probably related to δ, which increased from case 4 to case 5. The δ_{rms}, however, decreased by almost half from case 4 to case 5. The more blunt lip damped the oscillations. Thus, u_{rel} also decreased, indicating that the average gas stagnation temperature aft of the shock should be lower for case 4 (Engblom 1996).

A decrease in the mean heat flux distribution was expected for case 5, based on the experimental ablation onset times, even though the numerical cavity stagnation temperature was slightly higher owing to the more slowly moving bow shock. The mean heat flux did, in fact, decrease dramatically with the increased cavity lip radius of case 5. Thus, the bluntness of the cavity lip seems to have a greater influence on the mean heat flux than does the relative velocity of the bow shock.

The bow shock oscillations seen in animations for case 5 again showed the shock hovering at its most forward and aft positions. This hovering is apparent in plateaux of the bow shock motion (figure 6). Inspection of multiple instantaneous pressure contours shows that the pressure waves are coalescing into a cavity shock, but apparently closer to the cavity mouth than for the sharper cavity lip case (case 4). As with case 4, the shock formation again causes high-frequency, though lower-amplitude, oscillations in the instantaneous surface heat flux near the lip. Hence, 500 realizations in time were again required in order to calculate accurately the mean surface heat flux

distribution. The forward moving heat flux front is still present in case 5; however, it appears to be much weaker than it was for case 4. The instantaneous peak surface heat flux for case 5 occurs just downstream of the start of the cavity lip. The coincidence of the smaller peak instantaneous surface heat flux and the shock formation just at the cavity lip suggests that they are inter-related. Perhaps the high temperatures associated with the shock formation remain in the cavity for a shorter period of time as the gases near the cavity mouth are more quickly circulated away from the cavity lip, decreasing the duration of the heating and therefore the heat flux. The overall flow field for case 5 is very similar to that of case 4. Hence, the sole reason the mean peak surface heat flux decreased was the blunting of the cavity lip.

The decrease in mean surface heat flux distribution corresponds to a lower heat conduction coefficient boundary condition for the solid-body portion of the simulation. The solid-body heat conduction code predicts numerical ablation onset times of 2.7 s and 6.6 s for cases 4 and 5, respectively, assuming a $T_i = 100$ K. These numerical ablation onset times are much longer than the average experimental ablation onset times or even the best experimental run (table 3) for both geometries. If $T_i = 163$ K, the numerically predicted ablation onset times are reduced to 1.5 s and 3.6 s, respectively, and agreement with experiments is much improved. The simulations predict ablation onset 0.1 s (6%) earlier than the experimental average for case 4 and 0.7 s (24%) later than the average for case 5. This is remarkably good agreement, suggesting that the initial temperature really was about 163 K. Finally, the numerical simulations substantiate that a blunt lip geometry will indeed delay ablation onset well beyond that of the baseline hemisphere–cylinder geometry while a similar sharp lip geometry will not (table 3).

4.3. *Cavity diameter*

4.3.1. *Experiments*

Having experimentally and numerically examined the effects of cavity length (as L/D) and cavity lip radius, it was necessary to determine the effect of varying cavity diameter and how the optimal lip radius varied with cavity diameter. Hence, a cavity diameter parameter study was begun.

Two additional cavity diameters, $D = 17.8$ mm and $D = 7.6$ mm, were investigated, in addition to the results already available. For $D = 17.8$ mm, the maximum cavity lip radius is 1.90 mm (figure 2*a*). For $D = 12.7$ mm, the maximum r is 3.17 mm and for $D = 7.6$ mm, the maximum r is 4.44 mm (figure 2*b*). Thus, three cavity lip radii were investigated at $D = 7.6$ mm ($r = 1.90$ mm, 3.17 mm and 4.44 mm), two at $D = 12.7$ mm ($r = 1.90$ mm and 3.17 mm), and only one at $D = 17.8$ mm ($r = 1.90$ mm). The cavity length was chosen such that a constant $L/D = 4.0$ was maintained. These geometries allowed the effect of cavity diameter to be determined independently of L/D as well as whether the optimal cavity lip radius determined previously was an absolute value or a relative value.

Looking at the experimental ablation onset times for $L/D = 4.0$ with various cavity diameter and lip radius (figure 11), it is quite apparent that ablation onset is most delayed for the greatest cavity lip radius possible for a given cavity diameter. The odd shape of the region shown in figure 11 results from the incomplete data available for this parameter space. Even with complete data available for the parameter space, the region would be triangular as the maximum lip radius possible decreases with increasing cavity diameter. Cases 5 ($D = 12.7$ mm, $r = 3.175$ mm, $L/D = 4.0$), 6 ($D = 7.62$ mm, $r = 4.445$ mm, $L/D = 4.0$) and 7 ($D = 17.78$ mm, $r = 1.905$ mm, $L/D = 4.0$) had comparable average ablation onset times, each of which delayed ablation onset

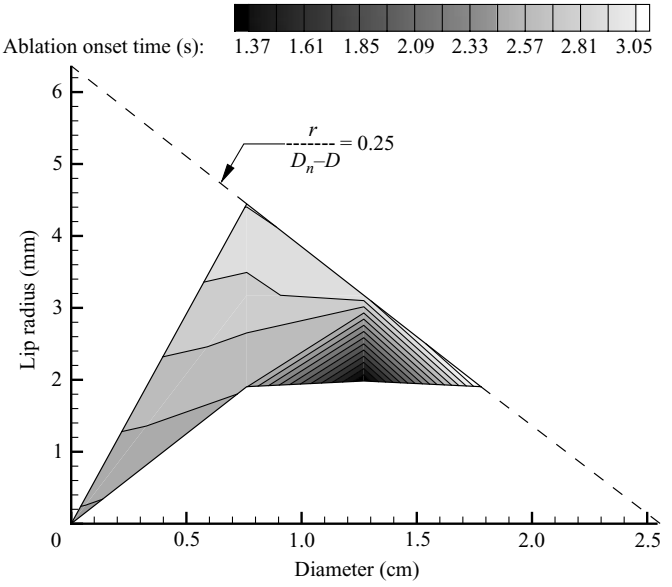

FIGURE 11. Ablation onset times for D parameter study with $L/D = 4.0$, where the dashed line indicates geometrical limit for $D_n = 25.4$ mm.

beyond that of the baseline hemisphere–cylinder geometry data (table 3). While the absolute cavity dimensions of these three geometries are significantly different, the relative dimensions are not. Each geometry has $L/D = 4.0$ and $r/(D_n - D) = 0.25$. That is, if $r/(D_n - D) = 0.25$, r is the geometrical maximum, which suggests that the optimal cavity lip radius is, in fact, a relative value and the geometrical maximum lip radius is best.

4.3.2. *Computations*

In order to determine why cases 5, 6 and 7 all significantly delayed experimental ablation onset times compared to those of the baseline hemisphere–cylinder body, these three geometries were investigated computationally. The numerical simulation for case 5 was discussed in § 4.2.2. The numerical simulations for cases 6 and 7 are discussed below and had the same temporal resolution requirements as case 5.

Unlike case 5, animations of the case 6 simulation show a continuous bow shock motion with no hovering at either its fore or aft positions. The continuous motion is also suggested by the sinusoidal shape of the cavity base pressure oscillations. The peak (maximum and minimum) pressures occur for a much shorter portion of the cycle and the change in pressure is much more gradual. However, δ_{rms} is tiny, and δ has decreased from that of case 5. In fact, the bow shock position is seen to change very little over the course of a cycle when compared to the other geometries (figure 6). If a theoretical frequency is calculated from (4.1) based on the stagnation temperature of the flow, the numerical simulation frequency is approximately 18% low. This discrepancy appears because the mean temperature in the cavity is much cooler than the stagnation temperature (figure 12) owing to convective cooling of the gas in the long narrow cavity. The temperature varies from 130 K at the cavity base to 370 K near the bow shock with the average temperature approximately 120 K below T_{stag}. If the theoretical frequency (4.1) is recalculated using an average cavity temperature of 250 K, it agrees with the numerical simulation frequency. As expected,

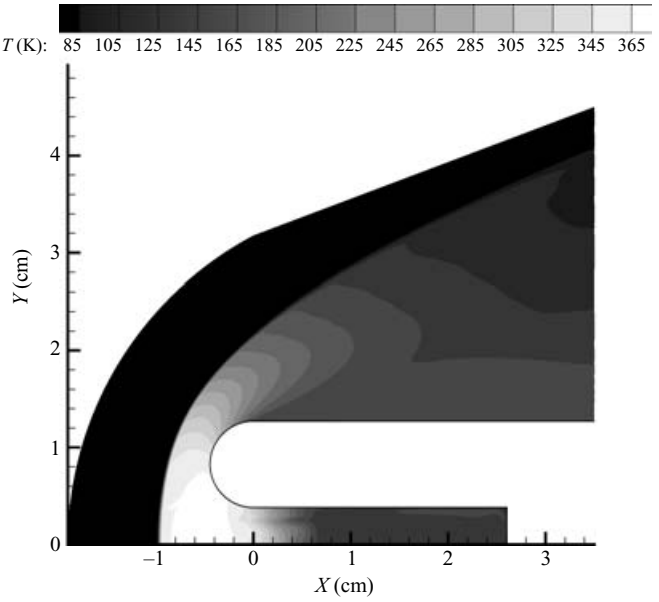

FIGURE 12. Mean temperature contours for case 6.

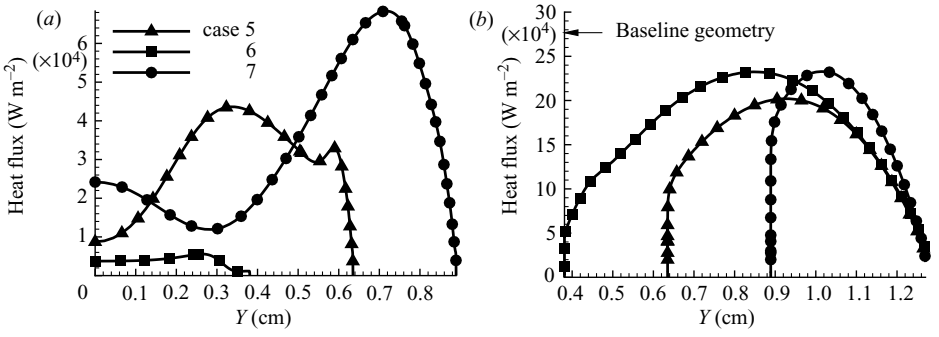

FIGURE 13. Mean heat flux comparison of cases 5, 6 and 7 along (*a*) the cavity base and (*b*) the cavity lip region. Note differences in vertical scales.

based on the limited motion and relatively high frequency, the relative velocity of the bow shock is very small.

As there is very little bow shock movement for case 6, there is also very little change in the instantaneous surface heat flux during a cycle. The instantaneous surface heat flux distribution remains quite smooth, as the tiny pressure waves in the cavity do not coalesce into a shock. The mean peak heat flux distribution around this blunt shape was found to be well below that of the baseline hemisphere–cylinder body, but slightly greater than the mean peak heat flux of case 5 (figure 13*b*). The heating at the base of the cavity is much smaller than near the lip (figure 13*a*, note vertical scales).

Case 7 is quite an interesting case: it is essentially a forward-facing thin-walled tube. The bow shock for this geometry hovers at its fore and aft positions with relatively quick movement between the two (figure 6). Figure 14 indicates that the pressure waves coalesce into a shock within the cavity during the late stages of inflow. The

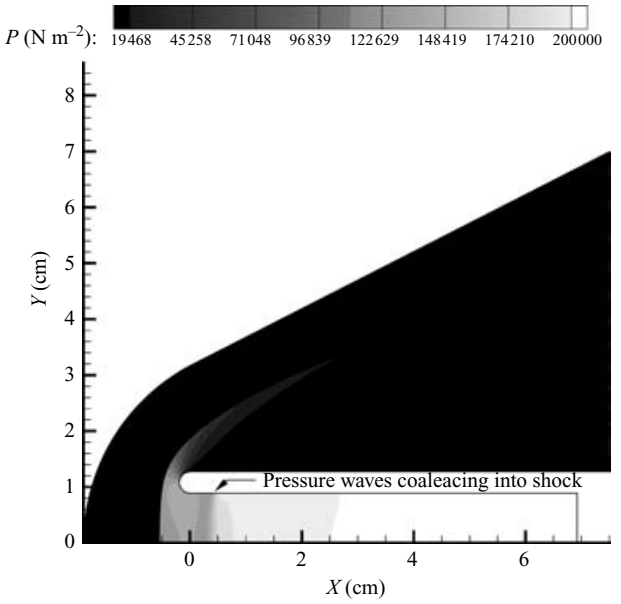

FIGURE 14. Pressure contours for case 7 as pressure waves begin to coalesce into a shock during cavity inflow.

simulated frequency of oscillation for case 7 was just 3.6% below the theoretically predicted value.

The δ and δ_{rms} for case 7 increased from that of case 5. The larger δ_{rms} is comparable to that found for other cavity geometries with comparably small lip geometries. This suggests that the amplitude of bow shock motion may be inversely related to cavity lip radius (i.e. sharper cavity lips have larger δ_{rms}), which would be in agreement with the sound radiation dissipation mechanism suggested by Engblom (1996) to drive the oscillations. The δ also appears to be influenced by cavity diameter as well as cavity lip radius. The computational results from the cavity lip radius parameter study suggest that δ increases with cavity lip radius for a constant cavity diameter. The cavity diameter results (presented in the current section) indicate that δ increases with D ($r/(D_n - D)$ held constant). Additionally, the relative velocity of the bow shock increased with an increase in cavity diameter and a corresponding increase in cavity length for a constant $L/D = 4.0$.

The instantaneous heat flux for case 7 begins to have abrupt fluctuations along the length of the cavity as the pressure waves coalesce into a shock within the cavity similar to the feature found for case 4. These fluctuations appear to grow in size as they (and the cavity shock) move upstream until the peak instantaneous heat flux is reached. The instantaneous peak heat flux corresponds with a dramatic thinning of the boundary layer as the forward-moving cavity shock passes over the cavity lip. If a way could be found to keep the boundary-layer thickness from decreasing so dramatically, it might be possible to decrease the average heat flux as well as the instantaneous heat flux. This in turn would delay ablation onset.

The position of the moving normal (cavity) shock is just upstream of where the curvature of the lip begins in figure 15. In this region, vorticity appears to be generated due to the baroclinic torque term in the boundary layer (figure 15, inset). Behind the normal shock, a small vortex has been generated and approaches the cavity lip. The

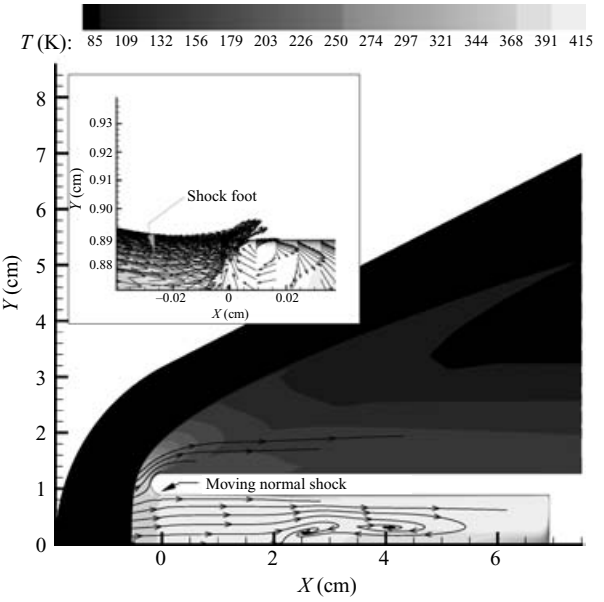

FIGURE 15. Temperature contours of case 7 corresponding to the instantaneous peak heat flux. Inset shows close-up of just inside the cavity lip with vectors.

extremely high heat flux associated with the wall normal jet at the forward portion of this vortex occurs for only an instant. Yet averaged over one oscillation period, the maximum mean surface heat flux is actually calculated to be below that of the baseline hemisphere–cylinder body. Figure 13(*b*) shows that the maximum mean surface heat flux in the region of the cavity lip for the thin-walled tube of case 7 was comparable to the maximum mean surface heat flux of the very blunt case 6, but greater than that of case 5.

The similarity of the maximum mean surface heat flux for these three geometries is remarkable considering the differences in the absolute geometries and the flow fields. In particular, while the maximum mean surface heat flux for each of these three geometries is lower than that of the baseline hemisphere–cylinder geometry, the recirculation region outside the cavity lip that was thought to cause the lower heat flux for sharp-lip shallow cavities (Engblom 1996; Yuceil 1995) is not present. Also, a large relative bow shock velocity, which was believed to decrease T_{stag} (Engblom 1996), does not necessarily indicate a low mean peak surface heat flux by itself. Instead, the most benefit accrues from a combination of δ, δ_{rms}, u_{rel}, r and D, all of which are intertwined.

The mean stagnation temperature fields of these three geometries show some notable trends (figure 16). First, the region of gas with a mean stagnation temperature above that of the free-stream value (370 K) thins and approaches the body as the cavity lip radius increases and the cavity diameter decreases. Secondly, the stagnation temperature field for case 6 begins to approach that of the baseline hemisphere–cylinder geometry (except in the cavity itself) supporting the idea that the flow is simply 'seeing' a blunter body and the weak oscillations are irrelevant. Thirdly, the mean stagnation temperatures close to the outer body and cavity lip are reduced in cases 5 and 7 owing to the bow shock oscillations. This is evidence that the mechanism previously thought to decrease heat flux (Engblom 1996) does indeed work to some

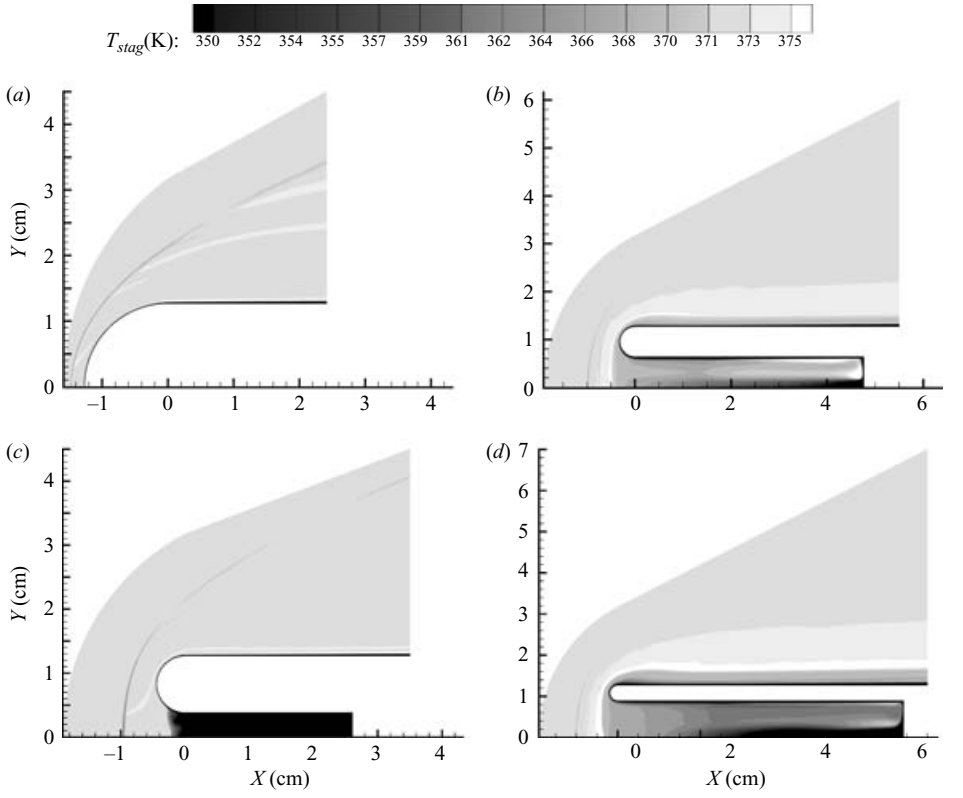

FIGURE 16. Mean stagnation temperature comparison of (*a*) baseline hemisphere–cylinder, and cavity geometries; (*b*) case 5, (*c*) case 6 and (*d*) case 7.

extent. Consistent with the findings of previous experimental and computational studies (Sambamurthi, Huebner & Utreja 1987; Huebner & Utreja 1987; Spring & Smith 1993), the mean heat flux at the base of the cavity (figure 13*a*) is much lower than that at the lip for all of these geometries.

Because of the large differences in body geometries, comparable maximum mean surface heat flux may not lead to comparable ablation onset times. In fact, numerical ablation onset occurs at 6.60 s, 5.66 s and 4.28 s for cases 5, 6 and 7, respectively, when an initial body temperature of 100 K is assumed. All of these numerical cavity ablation onset times are longer than the numerical ablation onset time of 3.73 s found for the baseline geometry with the same $T_i = 100$ K (figure 17). These numerical ablation onset times are longer than the experimental ablation onset times found for these geometries (table 3) indicating that the ice body warmed beyond 100 K by the time the shield was removed. Better agreement with the experimental findings is obtained when $T_i = 163$ K is used for the heat conduction computations.

As discussed is § 4.2.2, the numerical ablation onset time found for case 5 is 24% above the average experimental ablation onset time indicating that the body may have warmed even beyond 163 K. The numerical ablation onset time for case 6 ($T_i = 163$ K) agrees perfectly with the average experimental ablation onset time. This agreement is quite remarkable, further substantiating that the numerical assumptions are reasonable. The numerical ablation onset time found for case 7 is 22% below the average experimental onset time for $T_i = 163$ K and 35% above for $T_i = 100$ K

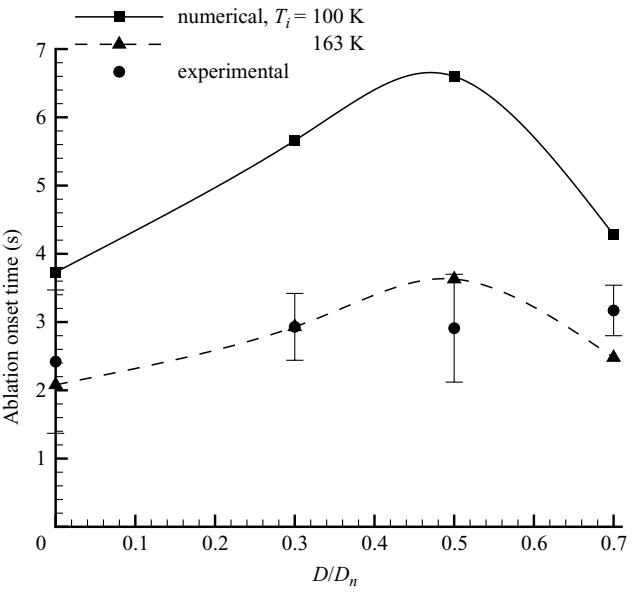

FIGURE 17. Dependence of ablation onset time on cavity diameter with $L/D = 4.0$, $r/(D_n - D) = 0.25$ and $D_n = 25.4$ mm (cases 5, 6 and 7). $D/D_n = 0$ is the baseline hemisphere–cylinder geometry. Experimental error as indicated.

suggesting that the body has probably warmed to only about 140 K. For a $T_i = 163$ K, as for a $T_i = 100$ K, the introduction of a forward-facing cavity, in the manner of cases 5, 6 and 7, delayed ablation onset beyond that of the similar baseline hemisphere–cylinder geometry (figure 17).

For application to a projectile in free flight, the actual percentage delay of ablation onset is best determined from the numerical ablation onset times for a given initial temperature since the projectiles will all have a constant uniform temperature prior to being launched. For a given initial temperature, case 5 delays ablation onset 75% over that of a baseline geometry of the same nose diameter whereas cases 6 and 7 delay ablation onset only 45% and 15%, respectively. Yet before we can consider a specific application on a projectile, aerodynamic drag must also be considered.

4.4. *Aerodynamic drag*

Although the nose cavity geometry occupies only a small region in the nose-tip, the effect on the drag is still of importance. For the three cases investigated in the numerical portion of the cavity diameter parametric study, the mean drag coefficient (i.e. drag averaged over one pressure oscillation cycle) increased as cavity diameter increased. The increase in drag seems to correspond to an increase in mean bow shock stand-off distance as a greater mean shock stand-off distance suggests that the flow 'sees' a blunter torpedo-shaped body. While these three geometries were found to delay ablation onset beyond that of the baseline hemisphere–cylinder body of the same nose-tip diameter, all incurred a penalty in drag ranging from 20% to 50% (a fit for these cases would be $C_D \approx 0.934 + 0.852 D/D_n$).

The question is then raised of whether or not ablation onset could be delayed to the same point in time as case 5 (the geometry that most delayed ablation onset) if a hemisphere–cylinder blunt body having the same absolute drag is used. Case 5 had a computed drag of 54.85 N. If an absolute drag of 54.85 N is deemed acceptable,

a simple larger hemispherical body 30.7 mm in diameter would have that drag ($C_D = 0.934$). For such a body with $D_n = 30.7$ mm, $q_{stag} = 251.6\,\mathrm{kW\,m^{-2}}$ was obtained from a numerical simulation of the flow field. This heat flux, while below that of the baseline blunt body ($D_n = 25.4$ mm), is greater than that of case 5 ($q_{stag} = 202\,\mathrm{kW\,m^{-2}}$). The solid-body heat conduction solver was then used to calculate the ablation onset time for $T_i = 100$ K and $T_i = 163$ K for this enlarged hemispherical shape. The numerical ablation onset times were found to be 4.63 s and 2.56 s, respectively. Thus, a blunter hemispherical nose can indeed delay ablation onset. However, the delay in ablation onset time for case 5 (6.60 s for $T_i = 100$ K and 3.63 s for $T_i = 163$ K) is still 42% greater with the same penalty in drag.

Thus, it has been shown that a delay in ablation onset can usefully be obtained by introducing a forward-facing cavity into the nose-tip of a hypersonic projectile. The question of how to pay the drag penalty is up to the designer. If we want the nose-tip diameter to remain constant, as a forward-facing cavity is used to delay ablation onset, a penalty in drag will have to be accepted. However, if an increase in drag is unacceptable, the introduction of a forward-facing cavity into a nose-tip of slightly smaller diameter (20% with the current geometry) will still significantly delay ablation onset without increasing nose-tip drag.

5. Summary and conclusions

A combined numerical and experimental investigation of ablation onset in unsteady hypersonic flow about nose-tips with a forward-facing cavity was presented. The geometries for both portions of the investigation consisted of a hemisphere–cylinder body with a cylindrical cavity. All cavity geometries investigated fell well within the regime of self-sustained pressure (and bow shock) oscillations even in a quiet free stream. Experiments and simulations were used in a coordinated and complementary effort. The geometric parameters believed to influence ablation onset most have been investigated. Experimental images and ablation onset times along with numerically derived flow images and animations provided substantial insight into the effect of these parameters on heat flux, and hence ablation onset times.

The parametric study investigated the effect of cavity length, cavity lip radius and cavity diameter on the ablation onset times. Each parameter was first investigated experimentally and independently optimized. Time-intense numerical simulations were then completed for the geometries indicating the most delayed ablation onset relative to the other geometries investigated.

A foward-facing nose-tip geometry was found that could delay ablation onset beyond that of the baseline hemisphere–cylinder nose-tip. It was found that the best cavity length, for a given nose diameter, was four times the cavity diameter. The best cavity lip radius was a quarter of the difference between the nose diameter and the cavity diameter. Using the optimal relative values for cavity length and the cavity lip radius, the effect of cavity diameter on the maximum mean heat flux and experimental ablation onset times was small. The numerical results suggested that the cavity diameter that most increased ablation onset time, with both cavity length and cavity lip radius optimized, was half the nose diameter.

Unfortunately, use of this optimized geometry would incur a drag penalty. However, it was shown that ablation would occur sooner for a blunter hemispherical geometry (having the same absolute drag as the optimized forward-facing cavity geometry) than for the optimized forward-facing cavity geometry. Thus, the introduction of a

forward-facing cavity can indeed be used to delay ablation onset, without increasing drag, by slightly decreasing the nose-tip diameter.

The authors are grateful to Scott Imlay and Moeljo Soetrisno, AMTEC Engineering, for their technical support on INCA, and to Roy Hogan and W. Hugh Walker of Sandia National Laboratories for their help with COYOTE. The authors would like to acknowledge the ARL MSRC for the use of their T90 and SGI and the TACC at the University of Texas at Austin for use of their CRAY J90 and SV1 for the numerical aspects of this project. The authors would also like to thank James Sanders and Travis Cook for their help with the experimental design. This work was supported in part by the Institute for Advanced Technology under US Army Research Laboratory contract DAAA21-93-C-0101 and a National Science Foundation Graduate Fellowship.

REFERENCES

Bastianon, R. A. 1968 Steady and unsteady solution of the flow field over concave bodies in a supersonic free stream. *AIAA Paper* 68-946.

Blacker, T. D. 1988 Fastq users manual version 1.2. *Tech. Rep.* SAND88-1326. Sandia National Laboratories.

Bohachevsky, I. O. & Kostoff, R. N. 1972 Supersonic flow over convex and concave shapes with radiation and ablation effects. *AIAA J.* **10**, 1024–1031.

Childs, G. E., Ericks, L. J. & Powell, R. L. 1973 *Thermal Conductivity of Solids at Room Temperature and Below*. National Bureau of Standards.

Engblom, W. A. 1996 Numerical investigation of hypersonic flow over a forward-facing cavity. PhD thesis, The University of Texas, Austin.

Engblom, W. A. & Goldstein, D. B. 1996 Nose-tip surface heat reduction mechanism. *J. Thermophys. Heat Transfer* **10**, 598–606.

Engblom, W. A., Goldstein, D. B., Ladoon, D. & Schneider, S. P. 1997 Fluid dynamics of hypersonic forward-facing cavity flow. *J. Spacecraft Rockets* **34**, 437–444.

Engblom, W. A., Yuceil, B., Goldstein, D. B. & Dolling, D. S. 1996 Experimental and numerical study of hypersonic forward-facing cavity flow. *J. Spacecraft Rockets* **33**, 353–359.

Gartling, D. K. & Hogan, R. E. 1994 Coyote – a finite element computer program for nonlinear heat conduction problems, part 1 – theoretical background. *Tech. Rep.* SAND94-1173. Sandia National Laboratories.

GRIDALL 1994 Gridall user's manual version 1.0. Amtec Engineering.

Hartmann, J. & Troll, B. 1922 On a new method for the generation of sound waves. *Phys. Rev.* **20**, 719–727.

Hassan, B., Kuntz, D. W. & Potter, D. L. 1998 Coupled fluid/thermal prediction of ablating hypersonic vehicles. *AIAA Paper* 98-0168.

Hobbs, P. V. 1974 *Ice Physics*. Clarendon.

Huebner, L. D. & Utreja, L. R. 1987 Experimental flowfield measurements of a nose cavity configuration. *SAE Paper* 871880.

Imlay, S. T., Roberts, D. W., Soetrisno, M. & Eberhardy, S. 1998 Inca user's manual version 2.5. Amtec Engineering.

Johnson, R. H. 1959 Instability in hypersonic flow about blunt bodies. *Phys. Fluid* **2**, 526–532.

Johnson, V. J. 1961 *Properties of Materials at Low Temperature*. Pergamon.

Kuntz, D. W., Hassan, B. & Potter, D. L. 1999 An iterative approach for coupling fluid/thermal predictions of ablating hypersonic vehicles. *AIAA Paper* 99-3460.

Ladoon, D., Schneider, S. & Schmisseur, J. 1998 Physics of resonance in a supersonic forward-facing cavity. *J. Spacecraft Rockets* **35**, 626–632.

Reinecke, W. G. & Guillot, M. J. 1995 Full scale ablation testing of candidate hypervelocity nose tip materials. In *Proc. of the 15th Intl Symp. on Ballistics*.

Reinecke, W. G. & Sherman, M. 1993 Tip survivability and performance on hypervelocity projectiles. In *Proc. of the 14th Intl Symp on Ballistics*.

Sambamurthi, J. K., Huebner, L. D. & Utreja, L. R. 1987 Hypersonic flow over a cone with nose cavity. *AIAA Paper* 87-1193.

Silton, S. I. 2001 Ablation onset in unsteady hypersonic flow about nose-tip with a forward-facing cavity. PhD thesis, University of Texas, Austin.

Silton, S. I. & Goldstein, D. B. 2000 Ablation onset in unsteady hypersonic flow about nose tip with cavity. *J. Thermophys. Heat Transfer* **14**, 421–434.

Spring, S. A. & Smith, C. E. 1993 Numerical study of a hollow-nosed interceptor design. *AIAA Paper* 93-3630.

Yuceil, B. 1995 An experimental investigation of a forward-facing nose cavity on a blunt body at mach 5. PhD thesis, University of Texas, Austin.

Yuceil, B. & Dolling, D. S. 1996 IR imaging and shock visualization of flow over a blunt body with a nose cavity. *AIAA Paper* 96-0232.